

Direct numerical simulations of the κ -mechanism

II. Nonlinear saturation and the Hertzsprung progression

T. Gastine and B. Dintrans

Laboratoire d'Astrophysique de Toulouse-Tarbes, Université de Toulouse, CNRS, 14 avenue Edouard Belin, 31400 Toulouse, France
e-mail: thomas.gastine@ast.obs-mip.fr

Received 2 April 2008 / Accepted 24 July 2008

ABSTRACT

Context. We study the κ -mechanism that excites radial oscillations in Cepheid variables.

Aims. We address the mode couplings that manage the nonlinear saturation of the instability in direct numerical simulations (DNS).

Methods. We project the DNS fields onto an acoustic subspace built from the regular and adjoint eigenvectors that are solutions to the linear oscillation equations.

Results. We determine the time evolution of both the amplitude and kinetic energy of each mode that propagates in the DNS. More than 98% of the total kinetic energy is contained in two modes that correspond to the linearly-unstable fundamental mode and the linearly-stable second overtone. Because the eigenperiod ratio is close to 1/2, we discover that the nonlinear saturation is due to a 2:1 resonance between these two modes. An interesting application of this result concerns the reproduction of Hertzsprung's progression observed in Bump Cepheids.

Key words. hydrodynamics – instabilities – waves – stars: oscillations – stars: variables: Cepheids – methods: numerical

1. Introduction

In [Gastine & Dintrans \(2008\)](#) (hereafter Paper I), we modelled the κ -mechanism in classical Cepheids using a simplified approach, that is, the propagation of acoustic waves in a layer of gas where the opacity bump is represented by a hollow in radiative conductivity. To maintain the mode excitation, the two following conditions apply:

- a sufficient width and amplitude are required for the conductivity hollow;
- this hollow must be located in a precise zone called the “transition region”.

Our parametric approach enabled us to check the reality of these two conditions and to obtain the instability strips from a linear-stability analysis. By starting from the most favourable situations (i.e. the most unstable linear modes), we performed the corresponding 1D and 2D nonlinear Direct Numerical Simulations (hereafter DNS). These DNS confirmed with a noteworthy agreement both the growth rates and spatial structures of linearly-unstable modes. The nonlinear saturation was reached and a quantitative study of the involved mode couplings remained to be done.

This is the principle aim of this paper. To study the nonlinear interactions between modes, we adapt a powerful method used in, e.g., aeroacoustics ([Salwen & Grosch 1981](#); [Wang et al. 2006](#)) or numerical astrophysics ([Bogdan et al. 1993](#), hereafter BCM93). It is based on a projection of DNS fields onto a basis shaped from the regular and adjoint eigenvectors that are solutions to the linear oscillation equations. This method has already been used in a simplified version by one of us to study internal waves in DNS ([Dintrans & Brandenburg 2004](#);

[Dintrans et al. 2005](#)). In the quoted investigation the eigenvalue problem was adiabatic, and therefore *Hermitian*, and the authors only accounted for projections onto regular eigenfunctions. This reduction is not applicable in our κ -mechanism simulations since the transition region requires low densities close to the surface and then high diffusivities (Paper I). Eigenmodes are highly non-adiabatic and imply non-Hermitian oscillation operators with non-orthogonal eigenfunctions. Solving the adjoint problem is therefore mandatory to determine both mode amplitudes and energy.

By using projections onto the two respective sets of eigenvectors, the regular and adjoint ones, the time evolution of each acoustic mode propagating in DNS is completed. The kinetic energy in each acoustic mode is available that highlights the energy transfer between modes. One of the main results of this work is that more than 98% of the total kinetic energy is contained in both the fundamental mode and the second overtone. Because this second overtone is linearly stable, we show that its large amplitude results from a 2:1 resonance with the fundamental mode. In our numerical experiments, this resonance is efficient because the ratio of the two involved periods, that is P_2/P_0 , is close to 1/2.

This nonlinear saturation based on a 2:1 resonance is an interesting result because this mechanism has been proposed to explain the secondary bump in light curves of some classical Cepheids named “Bump Cepheids”. The bump position is correlated with the oscillation period that leads to the well-known *Hertzsprung progression* ([Hertzsprung 1926](#); [Payne-Gaposchkin 1954](#)). The bump first appears on the descending branch of the light curve of Population I Cepheids with periods of about 6–7 days and then travels up this curve to reach its maximum for

10–11 day Cepheids. For longer periods, it moves down in the ascending branch and disappears for periods longer than 20 days (Whitney 1983; Tsvetkov 1990; Bono et al. 2000). Two main theories have been developed to explain this phenomenon:

- Whitney (1956) suggested an “echo mechanism” that Christy (1968) developed in more detail. In this model, two radial-pressure waves (called Christy’s waves) moving in opposite directions are generated during compression phases in the HeII ionisation region. The pulse running downward reflects on the stellar core and reaches the surface at the next period during which the bump appears;
- the second explanation, known as the “resonance mechanism”, has been proposed by Simon & Schmidt (1976, hereafter SS76). The bump results from a resonance between the fundamental mode and the second overtone that is possible for a period ratio P_2/P_0 close to 1/2.

Three papers of Whitney (1983) and Aikawa & Whitney (1984, 1985) compared the echo and resonance theories. The basic idea was to consider both approaches as two complementary sides of the same physical process. Despite promising results on polytropes (Whitney 1983), the dynamical approach showed that the acoustic-ray formalism did not reproduce the “running waves” in Christy’s diagram. This implies that most of the energy is contained in standing waves rather than progressive waves (Aikawa & Whitney 1984, 1985).

The resonance mechanism has also been investigated using the amplitude-equations formalism by Buchler & Goupil (1984) and Klapp et al. (1985). They established the dominant role of a 2:1 resonance because phases and amplitudes of modes show characteristic variations with the period-ratio P_2/P_0 (see also Simon & Lee 1981; Kovacs & Buchler 1989; Buchler et al. 1990). Despite these results favoring the resonance phenomenon, the echo-resonance controversy remains topical (Fadeyev & Muthsam 1992; Bono et al. 2000, 2002).

It is interesting to know whether our model is able to reproduce this Hertzsprung progression. Up to 400 DNS are completed to cover a significant range in the P_2/P_0 ratio, while studying the bump position in luminosity curves. This allows us to accurately reproduce the expected bump-progression with the ratio value: (i) if $P_2/P_0 > 1/2$, the bump is located in the descending branch; (ii) if $P_2/P_0 < 1/2$, the bump is located in the ascending branch.

In Sects. 2 and 3, we introduce the general-oscillations equations and the associated adjoint problem, respectively. We develop our projection method and provide results in Sect. 4. Section 5 concerns the Hertzsprung progression and we outline our conclusions in Sect. 6.

2. The pulsation model and corresponding DNS

We focus on radial modes propagating in Cepheids and restrict our study to the 1D case. Our system, which represents a *local* zoom around an ionisation region, is composed of a layer of width d filled with a monatomic and perfect gas with $\gamma = c_p/c_v = 5/3$ (c_p and c_v are specific heats). Gravity $\mathbf{g} = -g\mathbf{e}_z$ and kinematic viscosity ν are assumed to be constant. Following Paper I, the ionisation region is described by a parametric hollow in radiative conductivity that corresponds to a bump in opacity. We recall below the temperature-dependent profile that is adopted for the radiative conductivity

$$K_0(T) = K_{\max} \left[1 + \mathcal{A} \frac{-\pi/2 + \arctan(\sigma T^+ T^-)}{\pi/2 + \arctan(\sigma e^2)} \right], \quad (1)$$

with

$$\mathcal{A} = \frac{K_{\max} - K_{\min}}{K_{\max}}, \quad T^\pm = T - T_{\text{bump}} \pm e, \quad (2)$$

where T_{bump} is the position of the hollow in temperature and σ , e and \mathcal{A} denote its slope, width and relative amplitude, respectively.

2.1. Instability strips from the linear-stability analysis

We are interested in small perturbations about the hydrostatic and radiative equilibria. The layer is fully radiative and the diffusion approximation implies that

$$\mathbf{F}' = -K_0 \nabla T' - K' \nabla T_0 \quad (3)$$

for the radiative flux perturbation (hereafter the “0” subscripts mean equilibrium quantities, while primes denote Eulerian ones).

Following Paper I, the depth d of the layer is selected as the length scale, and the top density ρ_{top} and temperature T_{top} as density and temperature scales, respectively. The velocity scale is thus $(c_p T_{\text{top}})^{1/2}$. Finally, gravity and fluxes are provided in units of $c_p T_{\text{top}}/d$ and $\rho_{\text{top}}(c_p T_{\text{top}})^{3/2}$, respectively. The linearised perturbations obey the following temperature, momentum and continuity dimensionless equations:

$$\left\{ \begin{array}{l} \lambda T' = \frac{\gamma}{\rho_0} \left(K_0 \frac{d^2 T'}{dz^2} + 2 \frac{dK_0}{dz} \frac{dT'}{dz} + \frac{d^2 K_0}{dz^2} T' \right) \\ \quad - (\gamma - 1) T_0 \frac{du}{dz} + \frac{F_{\text{bot}}}{K_0} u, \\ \lambda u = -\frac{\gamma - 1}{\gamma} \left(\frac{dT'}{dz} + \frac{d \ln \rho_0}{dz} T' + T_0 \frac{dR}{dz} \right) \\ \quad + \frac{4}{3} \nu \left(\frac{d^2 u}{dz^2} + \frac{d \ln \rho_0}{dz} \frac{du}{dz} \right), \\ \lambda R = -\frac{du}{dz} - \frac{d \ln \rho_0}{dz} u, \end{array} \right. \quad (4)$$

where $R \equiv \rho'/\rho_0$ denotes the density perturbation, u the velocity and F_{bot} the imposed bottom flux. Here we seek normal modes using a time-dependence of the form $\exp(\lambda t)$, with $\lambda = \tau + i\omega$ (τ is the damping or growth rate of the mode and ω its frequency). Finally, by assuming rigid walls at both limits of the domain for the velocity, a perfect conductor at the bottom and a perfect insulator at the top for the temperature, we obtain the following boundary conditions

$$\left\{ \begin{array}{l} u = 0 \text{ for } z = (0, 1), \\ \frac{dT'}{dz} = 0 \text{ for } z = 0, \\ T' = 0 \text{ for } z = 1. \end{array} \right. \quad (5)$$

Equations (4), (5) define an eigenvalue problem

$$A \Psi_n = \lambda_n \Psi_n, \quad (6)$$

where λ_n is the eigenvalue associated with the (complex) eigenvector $\Psi_n = (T', u, R)^T$. Here n defines the mode order, that is, the number of nodes of the eigenfunction u while the matrix A is

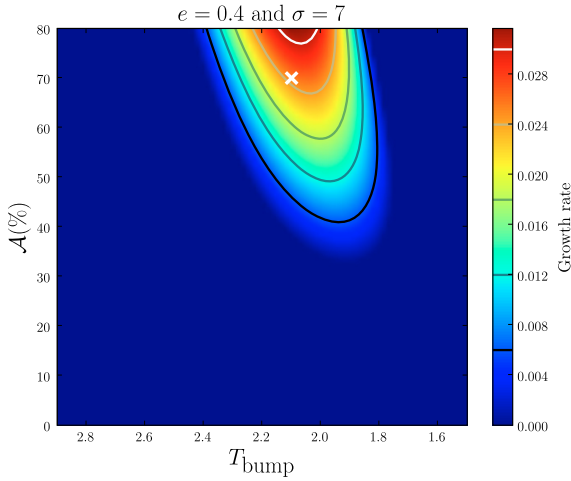


Fig. 1. Instability strip for the fundamental mode in the plane $(T_{\text{bump}}, \mathcal{A})$ for $e = 0.4$, $\sigma = 7$ and $\nu = 1 \times 10^{-4}$. The top (at $z = 1$) density and temperature are $\rho = 2.5 \times 10^{-3}$ and $T = 1$, respectively, while gravity is $g = 7$ everywhere. The white cross denotes a particular simulation further studied for $T_{\text{bump}} = 2.1$ and $\mathcal{A} = 70\%$.

a differential operator provided in Eq. (7), where the differential notation $D \equiv d/dz$ is used for clarity

$$A = \begin{pmatrix} \frac{\gamma}{\rho_0} (K_0 D^2 + 2DK_0 D + D^2 K_0) & -(\gamma - 1)T_0 D + \frac{F_{\text{bot}}}{K_0} & 0 \\ -\frac{\gamma - 1}{\gamma} (D \ln \rho_0 + D) & \frac{4}{3} \nu (D^2 + D \ln \rho_0 D) & -\frac{\gamma - 1}{\gamma} T_0 D \\ 0 & -D - D \ln \rho_0 & 0 \end{pmatrix}. \quad (7)$$

Figure 1 displays the instability strip for the fundamental mode¹. In this parametric survey, we fix the slope σ and width e of the conductivity hollow, whereas its amplitude \mathcal{A} and temperature T_{bump} vary (Eq. (1)). For every couple $(T_{\text{bump}}, \mathcal{A})$, both equilibrium fields and solutions to the eigenvalue problem (6) are completed using the LSB code (Linear Solver Builder, Valdetaro et al. 2007). Unstable modes with $\tau > 0$ are identified among all eigenvalues in each spectrum and only the fundamental mode is excited by the κ -mechanism in these simulations.

2.2. The associated nonlinear DNS

To confirm the reality of the instability strip and study the mode saturation, we perform a DNS of the nonlinear problem. We start from a linearly-unstable setup discovered in the parametric survey (the white cross in Fig. 1 of which the oscillation spectrum is provided in Table 1) and advance hydrodynamic equations in time using the Pencil-Code². Because we investigate the 1D case in this work, we cannot apply the 2D Alternate Direction Implicit (ADI) scheme developed in Paper I. We therefore code a 1D version of this scheme that consists of a semi-implicit Crank-Nicholson algorithm where nonlinearities are dealt with using a Jacobian factorisation (see e.g. Press et al. 1992, Sect. 16.6).

To determine which modes are present in the DNS once it has reached the nonlinear-saturation regime, we perform in Fig. 2a

¹ Figures are plotted using SciPy, open source scientific tools for Python (Jones et al. 2001–2008).

² See <http://www.nordita.org/software/pencil-code/> and Brandenburg & Dobler (2002).

Table 1. First linear eigenvalues of the unstable setup used to start the DNS (this setup is denoted by the white cross in the instability strip in Fig. 1). Note that only the fundamental $n = 0$ mode is linearly unstable.

mode order n	ω_n	$\tau_n (\times 10)$	period
0	5.439	+0.250	1.155
1	8.452	-1.816	0.743
2	11.06	-4.961	0.568
3	14.36	-4.727	0.437
4	17.40	-7.825	0.361
5	20.66	-9.363	0.304
6	23.82	-11.91	0.263

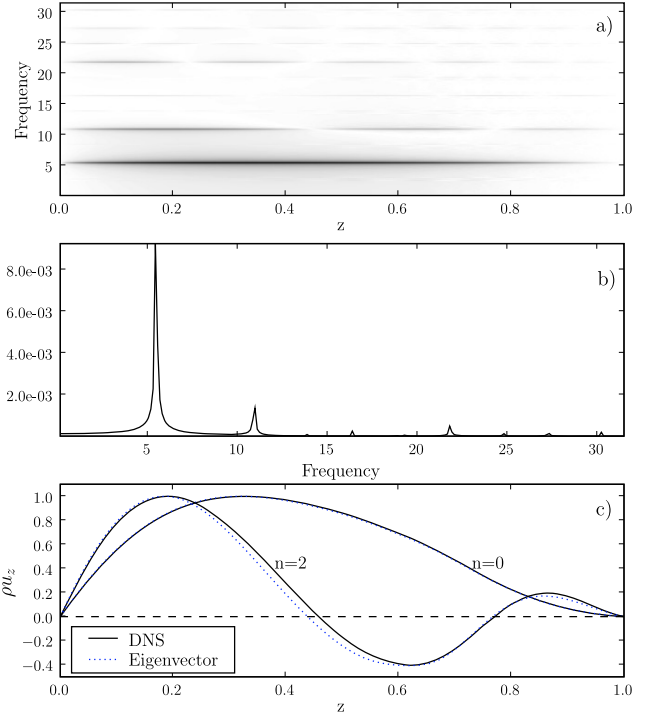


Fig. 2. a) Temporal power spectrum for the momentum in the (z, ω) -plane. b) The resulting spectrum after integrating over depth. c) Comparison between normalised momentum profiles for $n = (0, 2)$ modes according to the DNS power spectrum (solid black line) and to the linear-stability analysis (dotted blue line).

a temporal Fourier transform of the momentum field $\rho u(z, t)$ and plot the power spectrum in the (z, ω) -plane. With this method, acoustic modes are extracted because they emerge as “shark fin profiles” about definite eigenfrequencies (see Dintrans & Brandenburg 2004). In Fig. 2b, we integrate $\widehat{\rho u}(z, \omega)$ over depth to obtain the mean spectrum. Several discrete peaks corresponding to normal modes appear but the fundamental mode close to $\omega_0 = 5.439$ clearly dominates.

The linear eigenfunctions can be compared to the mean profiles computed from a zoom about given eigenfrequencies in the DNS power spectrum shown in Fig. 2. Figure 2c displays such profiles about $\omega_0 = 5.439$ and $\omega_2 = 11.06$ (solid black lines), whereas associated eigenfunctions are overplotted in dotted blue lines. The agreement between the linear-stability analysis and the DNS is remarkable.

In summary, Fig. 2 shows that several overtones are present in this DNS, even for long times. Because these overtones are linearly stable (see Table 1), some underlying energy transfers occur between modes. To investigate these intricate couplings in more detail, we need to follow the evolution of each mode *separately* using the projection method developed in the next section.

3. The adjoint problem

As said in the Introduction, the radiative diffusivity in our model is large close to the surface due to the instability criterion (the so-called “transition region” criterion). Eigenvectors strongly differ from adiabatic ones, and therefore the quasi-adiabatic approximation fails in this case. The dissipative effects must be fully taken into account and the oscillations operator is non-Hermitian. In other words, the matrix A provided in Eq. (7) is not self-adjoint and its eigenvectors Ψ_j are not mutually orthogonal. This implies that they cannot be used to arrange an acoustic subspace on which the physical fields of the DNS are projected. We thus consider the adjoint problem that has the same spectrum, while its eigenvectors are orthogonal to A -ones because of the biorthogonality property (see Appendix A.1).

3.1. The adjoint matrix A^\dagger

We start from the following inner-product

$$\langle X, Y \rangle = \int_0^1 X^\dagger Y dz, \quad (8)$$

where \dagger denotes the Hermitian conjugate. The adjoint of the operator A is defined by (e.g. Löwdin 1983)

$$\langle X, AY \rangle = \langle A^\dagger X, Y \rangle. \quad (9)$$

The eigenvectors Φ_i of A^\dagger are normalised to verify (see Appendix A.1)

$$\langle \Phi_i, \Psi_j \rangle = \delta_{ij}, \quad (10)$$

where Φ_i are the eigenvectors of A^\dagger such that

$$\begin{cases} A\Psi_j = \lambda_j\Psi_j, \\ A^\dagger\Phi_i = \lambda_i^*\Phi_i. \end{cases} \quad (11)$$

The adjoint-matrix calculation is detailed in Appendix A.2 and the resulting A^\dagger is provided in Eq. (16). This corresponds to the following oscillation equations for the adjoint problem:

$$\left\{ \begin{aligned} \lambda T' &= \frac{\gamma K_0}{\rho_0} \left\{ \frac{d^2 T'}{dz^2} - 2 \frac{d \ln \rho_0}{dz} \frac{dT'}{dz} \right. \\ &\quad \left. + \left[-\frac{d^2 \ln \rho_0}{dz^2} + \left(\frac{d \ln \rho_0}{dz} \right)^2 \right] T' \right\} \\ &\quad + \frac{\gamma - 1}{\gamma} \left(\frac{du}{dz} - \frac{d \ln \rho_0}{dz} u \right), \\ \lambda u &= (\gamma - 1) T_0 \frac{dT'}{dz} + (2 - \gamma) \frac{F_{\text{bot}}}{K_0} T' - \frac{d \ln \rho_0}{dz} R \\ &\quad + \frac{dR}{dz} + \frac{4}{3} \nu \left[\frac{d^2 u}{dz^2} - \frac{d \ln \rho_0}{dz} \frac{du}{dz} - \frac{d^2 \ln \rho_0}{dz^2} u \right], \\ \lambda R &= \frac{\gamma - 1}{\gamma} \left(T_0 \frac{du}{dz} - \frac{F_{\text{bot}}}{K_0} u \right). \end{aligned} \right. \quad (12)$$

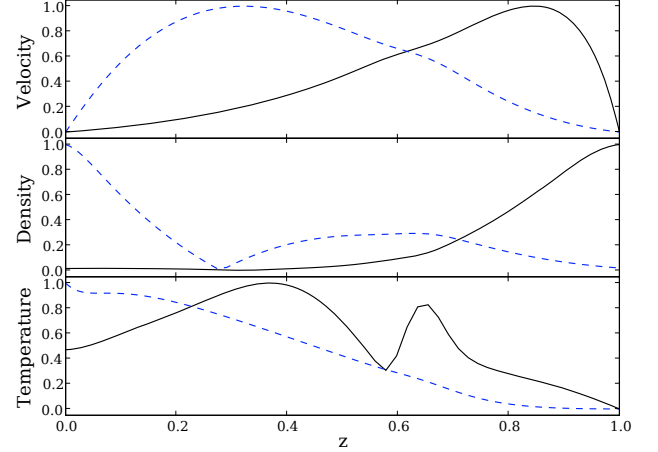


Fig. 3. Real part of normalised eigenfunctions (u , R , T') for the fundamental mode (solid black line) and its adjoint (dotted blue line), for the equilibrium setup denoted by a white cross in Fig. 1.

3.2. The adjoint boundary conditions

These boundary conditions are detailed in Appendix A.3. While integrating Eq. (A.6) by parts, we obtain surface contributions that must vanish to fulfill the adjoint definition (9) (Bohlius et al. 2007). This implies the following set of adjoint boundary conditions

$$\begin{cases} u = 0 \text{ for } z = (0, 1), \\ K_0 \frac{dT'}{dz} - \left(\frac{dK_0}{dz} + K_0 \frac{d \ln \rho_0}{dz} \right) T' = 0 \text{ for } z = 0, \\ T' = 0 \text{ for } z = 1. \end{cases} \quad (13)$$

3.3. Results

We solve the adjoint eigenvalue problem defined by Eqs. (12), (13) again using the LSB code, that is, we compute both the whole spectrum of eigenvalues λ_n^* and their associated eigenvectors Φ_n . An example is given in Fig. 3 where we plot the real part of both the regular (solid black line) and adjoint (dashed blue line) eigenfunctions of the fundamental $n = 0$ mode.

4. The projection method

Once the two sets of (regular) Ψ_n and (adjoint) Φ_n eigenvector are known, the DNS fields are projected at each timestep using the following procedure:

1. We first arrange the physical fields as

$$\Xi_{\text{DNS}}(z, t) = \begin{pmatrix} T' \\ u \\ R \end{pmatrix}_{\text{DNS}}, \quad (14)$$

where $u(z, t)$ is the velocity and $T'(z, t)$, $R(z, t)$ the temperature and density perturbations provided by

$$T'(z, t) = T(z, t) - T_0(z), \quad R(z, t) = \frac{\rho'}{\rho_0} = \frac{\rho(z, t)}{\rho_0(z)} - 1. \quad (15)$$

$$A^\dagger = \begin{pmatrix} \frac{\gamma K_0}{\rho_0} [D^2 - 2D \ln \rho_0 D + -D^2 \ln \rho_0 + (D \ln \rho_0)^2] & \frac{\gamma - 1}{\gamma} (D - D \ln \rho_0) & 0 \\ (\gamma - 1)T_0 D + (2 - \gamma) \frac{F_{\text{bot}}}{K_0} & \frac{4}{3} \nu (D^2 - D \ln \rho_0 D - D^2 \ln \rho_0) & D - D \ln \rho_0 \\ 0 & \frac{\gamma - 1}{\gamma} \left(T_0 D - \frac{F_{\text{bot}}}{K_0} \right) & 0 \end{pmatrix} \quad (16)$$

2. We decompose these fields onto the *regular*-linear eigenvectors

$$\Xi_{\text{DNS}}(z, t) = \Re \left\{ \sum_{n=0}^{\infty} c_n(t) \Psi_n(z) \right\}, \quad (17)$$

where the $c_n(t)$ coefficients are completed using *adjoint* eigenvectors

$$c_n(t) = \langle \Phi_n, \Xi_{\text{DNS}} \rangle = \int_0^1 \Phi_n^\dagger \Xi_{\text{DNS}} dz. \quad (18)$$

This complex function $c_n(t)$ defines the mode amplitude because its time evolution is related to the eigenfrequency ω_n by

$$c_n(t) = |c_n(t)| e^{i\phi_n(t)} \text{ with } \phi_n(t) \propto \omega_n t. \quad (19)$$

3. We perform Fourier transforms or phase diagrams of these $c_n(t)$ coefficients to investigate the evolution of modes.

4.1. Time evolution of the complex-mode amplitudes $c_n(t)$

The left panels of Fig. 4 show the time evolution of the real part of the projection coefficients $c_n(t)$ for the first four modes $n \in \llbracket 0, 3 \rrbracket$. We overplot the curves $\propto \exp(\tau_n t)$ derived from the linear-stability analysis (see Table 1). As expected, only the fundamental mode amplitude $c_0(t)$ grows at each timestep. For other linearly-stable modes, amplitudes decay except for the $n = 2$ one. The amplitude of this mode shows a transient decrease until time $t \approx 10$ and then begins to increase. This behaviour is an estimate of the nonlinear coupling that occurs between this overtone and (at least) the fundamental mode.

We next perform Fourier transforms of these mode amplitudes (right panel of Fig. 4). Following Eq. (19), the $c_n(t)$ amplitudes behave as $c_n(t) \propto \exp(i\omega_n t)$ because theoretical eigenfrequencies and peaks appearing in power spectra overlap one another.

4.2. Phase diagrams

In each panel of Fig. 5, the imaginary part of the complex mode amplitude $c_n(t)$ is plotted as a function of the real part for the four modes shown in Fig. 4. To avoid unreadable plots, we stop the time evolution at $t = 50$. The decreasing orbits are plotted as black lines, whereas the increasing ones are in blue. In these diagrams, the radius of each trajectory is related to the modulus of the complex mode amplitude, which implies that a decreasing (increasing) radius is associated with a damped (excited) mode.

Once again, the fundamental mode appears to be continuously excited. We note that the excitation phenomenon is coherent in the sense that no discontinuity is observed in the mode orbits, that is, the spiral develops continuously. For the second overtone, after the linearly-transient decrease, the radius begins

to increase significantly and this is still the signature of a nonlinear coupling with the fundamental mode. For the linearly-stable $n = 1$ and $n = 3$ modes, things are more intricate because a marginal increase is shown during the last orbits (also seen in Fig. 4). Unfortunately, these phase diagrams are not adapted to investigate this long-time dynamics because orbits will overlap one another.

4.3. The mode kinetic energy content

To address the mode couplings responsible for the nonlinear limit-cycle stability observed at late times, we compute the energy content of each mode separately.

In BCM93, the total amount of sound generated by the turbulent convection is weak because they find that only 0.22% of the kinetic energy is stored in acoustic standing waves. Our problem however consists of an initially static radiative zone without convection and the velocity field that develops is only due to acoustic modes, that is,

$$E_{\text{kin}}^{\text{tot}} = E_{\text{waves}} = \sum_{n=0}^{\infty} E_n, \quad (20)$$

where E_n is the kinetic energy contained in the n -acoustic mode. One advantage of our projection method lies in its ability to compute this kinetic energy content E_n because Eq. (17) implies that

$$u_{\text{DNS}} = \Re \left\{ \sum_{n=0}^{\infty} c_n(t) u_n \right\}, \quad (21)$$

where u_{DNS} and u_n are the velocity of the DNS and the regular eigenvector, respectively. By multiplying by $1/2\rho_0 u$, the kinetic energy density $E_{\text{kin}}(z)$ is obtained as

$$\begin{aligned} E_{\text{kin}}(z) &= \frac{1}{2} \rho_0 \Re \left\{ \sum_{n=0}^{\infty} c_n(t) u_n \right\} \Re \left\{ \sum_{p=0}^{\infty} c_p(t) u_p \right\} \\ &= \sum_{n=0}^{\infty} \sum_{p=0}^{\infty} \frac{1}{2} \rho_0 \Re [c_n(t) u_n] \Re [c_p(t) u_p]. \end{aligned} \quad (22)$$

After integrating over the domain, the total kinetic energy reads

$$E_{\text{kin}}^{\text{tot}} = \sum_{n=0}^{\infty} \left(\sum_{p=0}^{\infty} \frac{1}{2} \int_0^1 \rho_0 \Re [c_n(t) u_n] \Re [c_p(t) u_p] dz \right). \quad (23)$$

It is possible to determine the contribution of each acoustic mode to the whole amount of kinetic energy because Eq. (20) allows us to define E_n as

$$E_n = \sum_{p=0}^{\infty} \frac{1}{2} \int_0^1 \rho_0 \Re [c_n(t) u_n] \Re [c_p(t) u_p] dz. \quad (24)$$

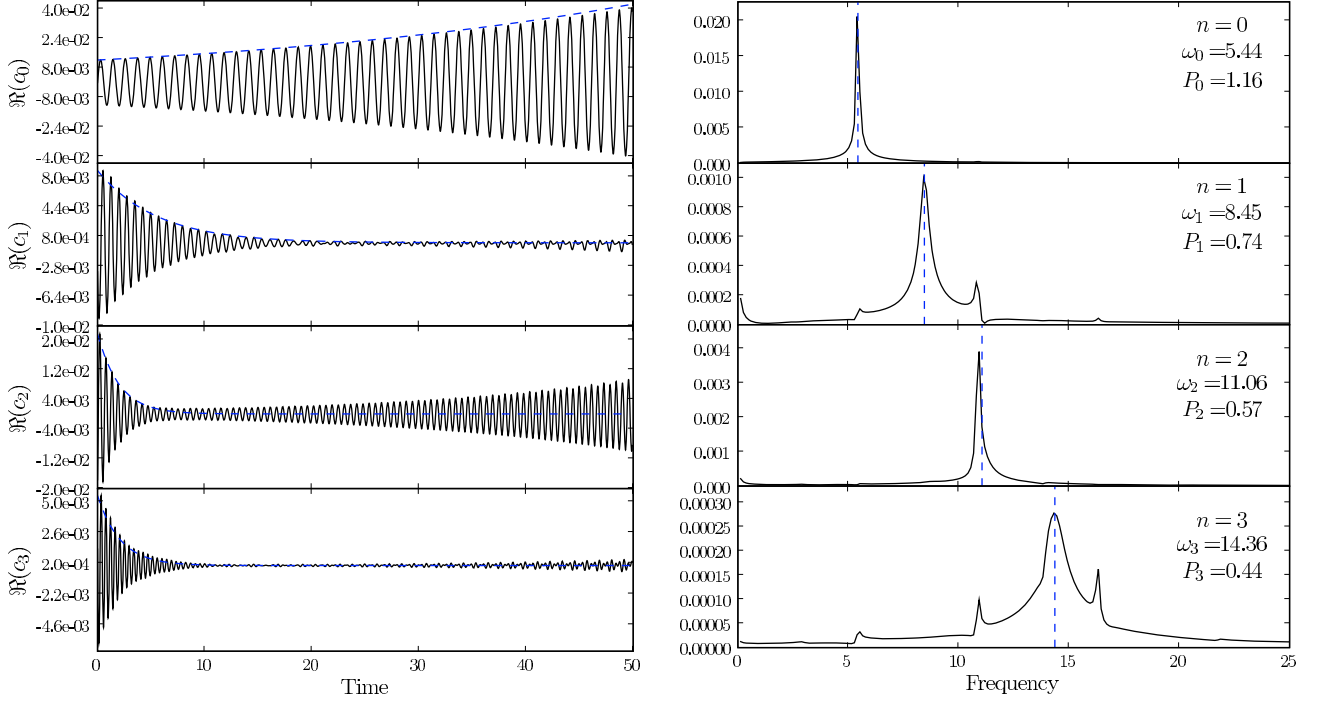


Fig. 4. *Left panel:* time evolution of the real part of the complex-mode amplitudes $c_n(t)$ for $n \in \llbracket 0, 3 \rrbracket$ modes. The theoretical growth or damping curves are overlotted in dashed blue lines. *Right panel:* their respective Fourier transforms. The modes eigenfrequencies are overlotted in dashed blue lines.

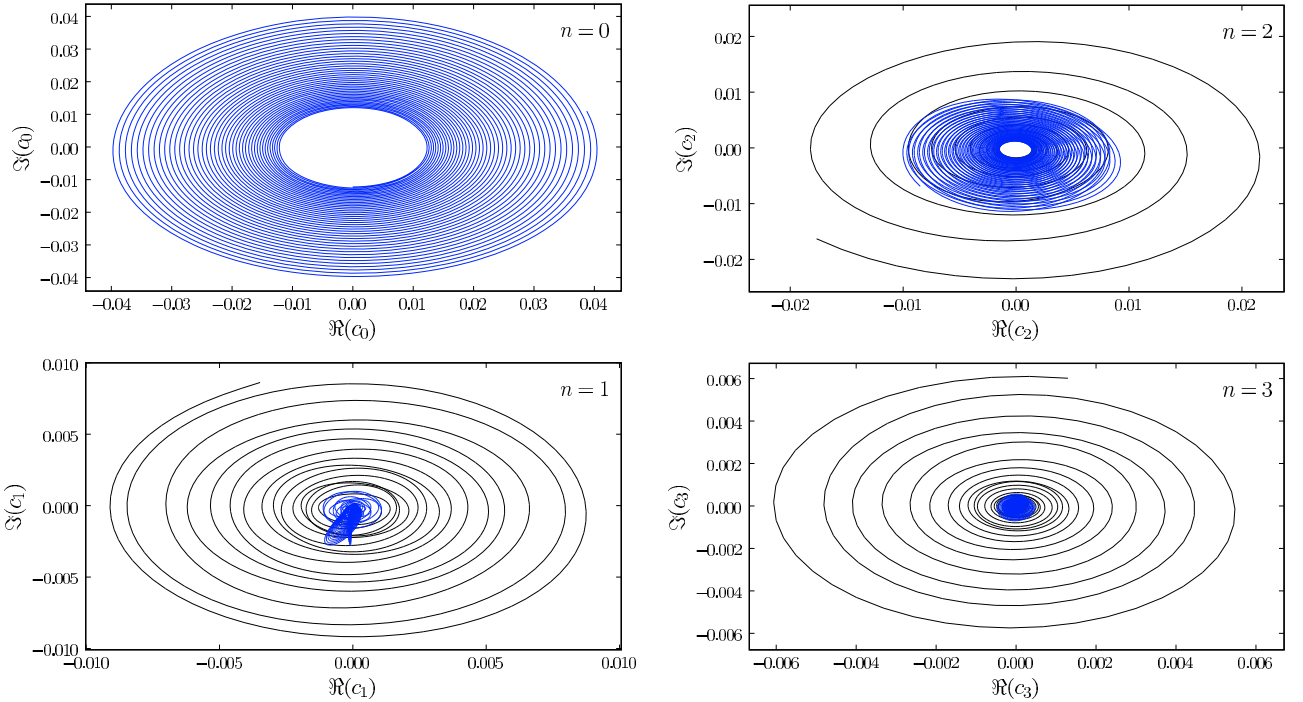


Fig. 5. Phase diagrams for $n \in \llbracket 0, 3 \rrbracket$ modes. The abscissa (ordinate) corresponds to the real (imaginary) part of the complex mode amplitude $c_n(t)$. The increasing orbits are plotted in blue, whereas the decreasing ones are in black.

Figure 6a displays the long-time evolution of the kinetic energy ratio $E_n/E_{\text{kin}}^{\text{tot}}$ for $n \in \llbracket 0, 6 \rrbracket$. After the transient linear growth of the fundamental mode, a given fraction of energy is progressively transferred to upper overtones and the nonlinear saturation is achieved above $t \approx 150$. These nonlinear couplings mainly involve the $n = 0$ and $n = 2$ modes because their energy ratios are dominant. However, the other overtones (i.e. $n \in \llbracket 1, 3-6 \rrbracket$)

also participate in this nonlinear saturation process but their energy ratios remain below 1%. This is compatible with the weak peaks around the corresponding frequencies ω_n shown in the power spectrum in Fig. 2b or with the marginal increase of the radius orbits in Fig. 5. It is at first glance not surprising because a high-order mode is associated with smaller scales and therefore with a high damping rate (Table 1). This implies that the

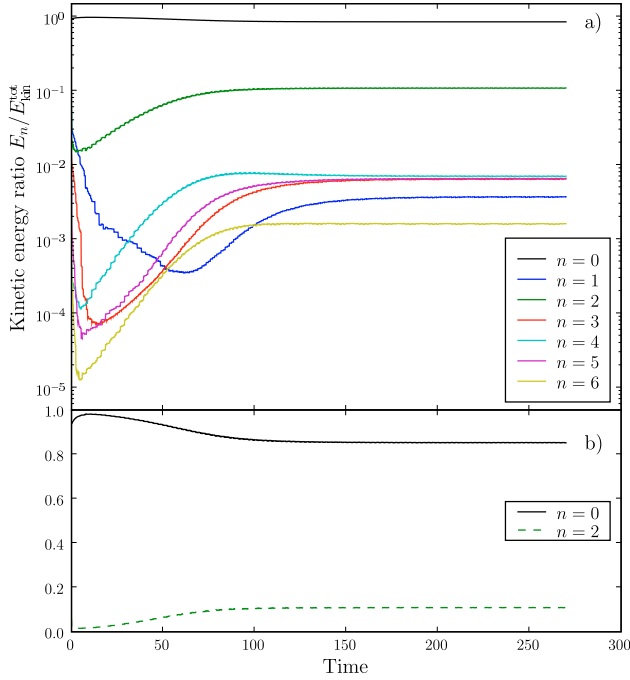


Fig. 6. **a)** Kinetic energy ratios for $n \in \llbracket 0, 6 \rrbracket$ in a logarithmic y -scale. **b)** Zoom in the $n = 0$ (solid black line) and $n = 2$ (dashed green line) mode energy contents.

excitation of these overtones from the fundamental mode would require efficient underlying couplings that are not observed in this simulation.

The fact that the $n = 2$ mode is more excited than the $n = 1$ one nevertheless contradicts this explanation because its damping rate is more than twice the $n = 1$ one. In Fig. 6b, we expand Fig. 6a for the fundamental mode and this second overtone only. The major energy transfer well occurs between these two modes because they contain about 98% of the total kinetic energy of this DNS. The reason for this favored coupling lies in the period ratio existing between these two modes (see Table 1): the fundamental period is $P_0 = 2\pi/\omega_0 \simeq 1.155$, while the $n = 2$ one is $P_2 \simeq 0.568$ such that the corresponding period ratio is close to one half ($P_2/P_0 \simeq 0.491$). The $n = 2$ mode therefore receives in a preferential way some energy from the $n = 0$ mode every two periods and that corresponds, from a dynamical point of view, to a classical 2:1 resonance. Such a resonance is usual in celestial mechanics with, e.g., Jupiter’s moons Io ($P = 1.769$ d), Europa ($P = 3.551$ d) and Ganymede ($P = 7.154$ d) and it is well known that it helps to stabilise orbits. In our case, this stabilisation takes the form of a nonlinear saturation: the linear growth of the fundamental mode is balanced by the pumping of energy from the linearly-stable second overtone behaving as an energy sink. The final amplitudes give about 87% of the kinetic energy in the fundamental mode and 11% in the second overtone, the remaining 2 percent being in higher overtones as displayed in Fig. 6a.

5. The Hertzprung progression

The nonlinear saturation in our excitation model therefore results from a 2:1 resonance between the fundamental mode and the second overtone. As shown in the Introduction, this mechanism has also been proposed to explain the secondary bump observed in the luminosity variations of Bump Cepheids (SS76). An interesting correlation between the value of the ratio P_2/P_0 and the bump position was also emphasised leading to the

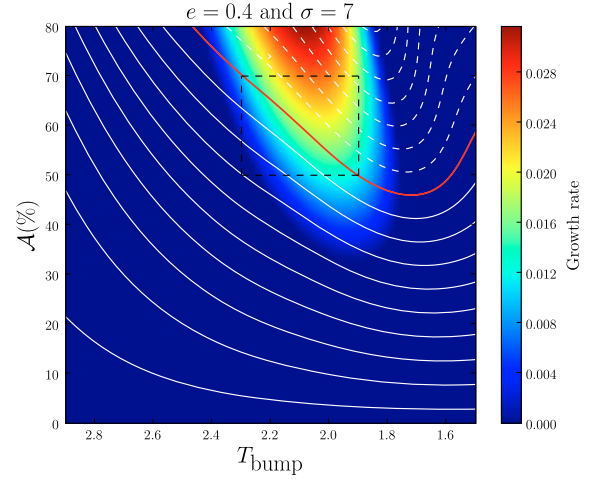


Fig. 7. P_2/P_0 level lines overlaid on the instability strip. Dashed white lines denote ratio $P_2/P_0 < 1/2$, while solid white lines correspond to $P_2/P_0 > 1/2$. The critical level $P_2/P_0 = 1/2$ is emphasised as a red line, and the dashed box delimits the region where a large number of DNS are performed to study Hertzprung’s progression (see Figs. 8, 9).

so-called “Hertzprung progression” (Simon & Lee 1981; Kovacs & Buchler 1989; Buchler et al. 1990). Nevertheless this correlation with P_2/P_0 is not observed as the period P_2 deduced from luminosity curves is *necessarily* equal to $P_0/2$. Indeed, the second overtone period changes due to nonlinear couplings and finally reaches the value $P_2 = P_0/2$ once the nonlinear saturation is achieved (i.e. the 2:1 resonance). As a consequence, only linear eigenperiods are relevant when studying the influence of the P_2/P_0 ratio on the bump position. Furthermore, Buchler et al. (1990) have shown that this correlation between the phase and the P_2/P_0 ratio is not reproduced in their models when plotting the phase as a function of P_0 only. As our hydrodynamical model deals with dimensionless quantities, studying the phase variations according to P_2/P_0 is also more consistent.

To determine whether our model is able to reproduce this Hertzprung progression, we first overplot in Fig. 7 the P_2/P_0 level lines with the instability strip discovered in the linear-stability analysis (Sect. 2.1). The solid white level lines correspond to $P_2/P_0 > 1/2$, the dashed lines to $P_2/P_0 < 1/2$ and the red line is for the critical level $P_2/P_0 = 1/2$. The instability strip is clearly split in two separate parts and the most unstable modes belong to the $P_2/P_0 < 1/2$ region. If we now perform the DNS corresponding to those different setups, we can check if the luminosity bump position is really correlated with the period ratio value. Because we are dealing with the 1D case, the luminosity reduces to the radiative flux at the top of the domain, that is,

$$L(t) \equiv F_{\text{top}}(t), \quad (25)$$

and the *luminosity curves* are transformed into *emerging radiative flux curves*. Because the bottom flux and the top temperature are imposed in the DNS, these flux variations $F_{\text{top}}(t)$ happen about F_{bot} .

We then run a large number of DNS (up to 400) in the instability strip to cover a significant range in the P_2/P_0 ratio and cross the 1/2-line; all these DNS belong to the dashed box shown in Fig. 7. In each case, the simulation is performed above the nonlinear saturation ($t_{\text{end}} = 500$). Because we know that the fundamental mode and the second overtone enter in the time

evolution of the emerging flux $F_{\text{top}}(t)$, we fit the obtained flux variations using the following decomposition:

$$f(t) = F_{\text{bot}} + A_0 \cos(\omega_0 t + \phi_0) + A_2 \cos(2\omega_0 t + \phi_2), \quad (26)$$

where the free parameters $[A_0, A_2, \phi_0, \phi_2]$ are computed using the Levenberg-Marquardt algorithm that is a nonlinear least-square method (e.g. Press et al. 1992, Sect. 15.5). The phase shift between the two signals is defined by

$$\Delta\phi = \phi_2 - 2\phi_0, \quad (27)$$

and allows first to phase the flux curves and second, to know where the secondary bump is. If $\Delta\phi$ is less (greater) than π , this secondary bump will be located in the descending (ascending) branch after (before) the flux maximum.

The whole DNS are summarised in Fig. 8 where isocontours of $\Delta\phi$ are plotted in the same $(T_{\text{bump}}, \mathcal{A})$ instability strip plane used in Fig. 7. The red regions are associated with $\Delta\phi > \pi$, the blue ones with $\Delta\phi < \pi$ and the white ones with $\Delta\phi = \pi$. By overplotting the level lines of the period ratio P_2/P_0 , the following correspondence appears:

$$\Delta\phi < \pi \text{ (bump after the max.)} \Leftrightarrow P_2/P_0 > 1/2,$$

$$\Delta\phi > \pi \text{ (bump before the max.)} \Leftrightarrow P_2/P_0 < 1/2, \quad (28)$$

which corresponds to the observed correlation (SS76).

To highlight this result, examples of light curves shaping an Hertzsprung progression are provided in Fig. 9. These eleven curves correspond to the black circles distributed across the $P_2/P_0 = 1/2$ level line in Fig. 8. The correspondences (28) appear clearly: the bump is located in the descending branch of the light curve if $P_2/P_0 > 1/2$, while values $P_2/P_0 < 1/2$ lead to a bump in the ascending branch.

Observations also show that the amplitude of the surface velocity presents a *double-peaked* behavior along the Hertzsprung progression as its center corresponds to a minimum value for the velocity (Bono et al. 2000). In our simulations, no clear correlation between the amplitude ratio A_2/A_0 and the bump position appears and we guess that it may be related to the two following restrictions:

- rigid walls for the velocity have been assumed. As we are interested in the physics involved near the top of the box, the ratio A_2/A_0 is not really relevant there compared to, say, the phase difference between the two modes;
- the sound speed contrast across the box is relatively weak. As the frequency step is given by $\Delta\nu \sim \left(2 \int_L dr/c_s\right)^{-1}$, there are not enough variations to obtain significant changes in this ratio.

However our model is able to qualitatively reproduce the Hertzsprung progression, as the position of the secondary bump with regard to the main bump evolves in the expected way with the P_2/P_0 ratio. We therefore conclude that the 2:1 resonance supplying the nonlinear saturation in our model results in an ‘‘observational’’ bump in the light curve of which the position is linked to the period ratio P_2/P_0 .

6. Conclusion

In this paper, we investigate the nonlinear saturation of the acoustic modes excited by the κ -mechanism in direct numerical simulations (DNS). This study follows on from our former work where we began our modelling of the κ -mechanism in Cepheids

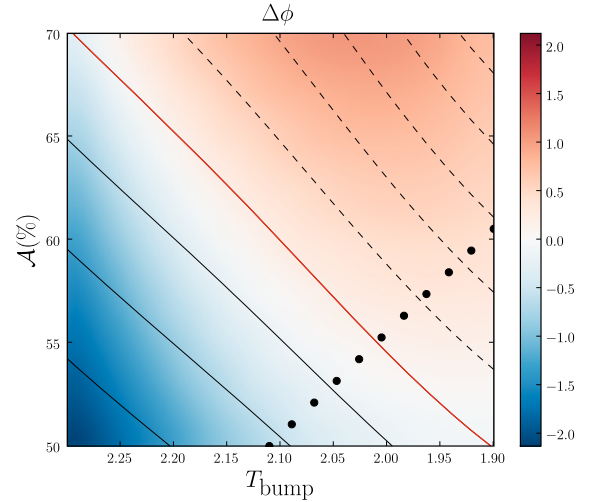


Fig. 8. Isocontours of $\Delta\phi$ in the $(T_{\text{bump}}, \mathcal{A})$ plane (note that we rather plot $\Delta\phi - \pi$ to highlight the critical line $\Delta\phi = \pi$). This figure corresponds to the dashed box in Fig. 7 and the black circles display eleven selected simulations showed in Fig. 9.

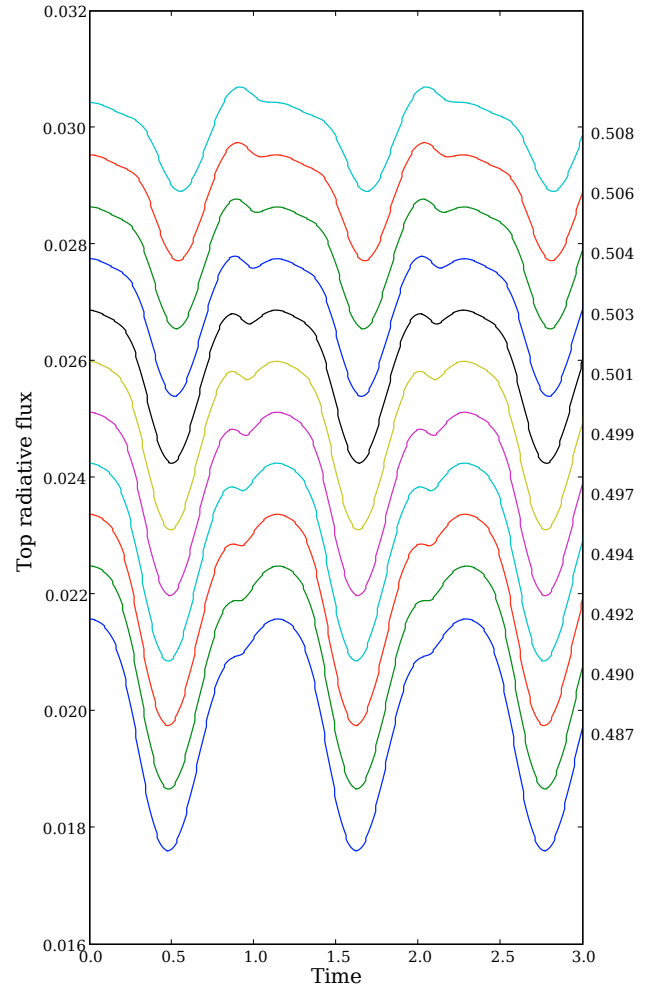


Fig. 9. Rephased time evolutions of the surface radiative flux about time $t = 500$ for the eleven selected simulations plotted as black circles in Fig. 8. The ratio of eigenperiods P_2/P_0 is indicated in each case.

by looking the propagation of acoustic modes in a layer of gas in which the ionisation is modelled by a hollow in the radiative conductivity profile (Gastine & Dintrans 2008, Paper I).

To catch the evolution of linearly-unstable modes, we apply an original method consisting of the projection of the DNS fields onto the eigenmodes that are solutions to the linear oscillation equations (Dintrans & Brandenburg 2004). Because the oscillation operator is non-Hermitian, the regular eigenvectors are not mutually orthogonal and we consider the adjoint problem that has the same spectrum while its eigenvectors are orthogonal to the regular ones. Thanks to these two sets of eigenvectors, we compute the projection coefficients for each DNS snapshot and follow the temporal evolution of acoustic modes separately. Corresponding phase diagrams show that the orbit radius of the *linearly*-unstable fundamental mode is continuously growing with time. On the contrary, orbits associated with the *linearly*-stable overtones exhibit decreasing radii, except the $n = 2$ one that is increasing at late times.

We derive the kinetic energy contributions of each mode propagating in the DNS. More than 98% of the total kinetic energy is contained in two modes corresponding to the fundamental mode and the second overtone. This last mode, which represents about 10% of the total kinetic energy, is involved in the nonlinear saturation of the instability through a 2:1 resonance with the fundamental mode. It means that the unstable fundamental mode gives energy to the stable second overtone that leads to the limit-cycle stability, as displayed in Fig. 6.

This 2:1 resonance is striking because the same mechanism is probably responsible for the observed bump in the luminosity curves of Bump Cepheids, leading to the well-known ‘‘Hertzsprung’s progression’’. This progression links the bump position to the period ratio P_2/P_0 existing between the fundamental mode and the second overtone (SS76). We perform a large number of DNS covering a significant range in this ratio and extract the resulting luminosity curves. The 2:1 resonance does lead to an Hertzsprung progression as the bump arises in the ascending branch for $P_2/P_0 < 1/2$, while it is located in the descending branch for $P_2/P_0 > 1/2$.

The study of the κ -mechanism in a purely-radiative layer is now completed with this work. The physical criteria for the instability as well as the nature of its nonlinear saturation are addressed. Future works will be devoted to the influence of convection on the mode stability. Indeed, a coupling between the convection and pulsations is suspected to play a major role in the disappearance of unstable modes close to the red edge of Cepheids’ instability strip. Time-dependent theories of convection have difficulty in explaining the red-edge location since they rely on many unconstrained parameters (e.g. Wuchterl & Feuchtinger 1998; Yecko et al. 1998). Because DNS fully account for crucial nonlinearities, they are appropriate to properly investigate this dynamical coupling between the acoustic modes and convection. We thus plan to perform 2D DNS of the κ -mechanism in the presence of convection. The interesting cases will of course correspond to a (local) convective-turnover timescale of the same order as the period of the fundamental mode.

Acknowledgements. We thank the referee (G. Bono) for his fruitful comments. Calculations were carried out on the CalMip machine of the ‘‘Centre Interuniversitaire de Calcul de Toulouse’’ (<http://www.calmip.cict.fr/>) and Grid’5000, which is an initiative from the French Ministry of Research through the ACI GRID incentive action, INRIA, CNRS and RENATER and other contributing partners (see <https://www.grid5000.fr>).

Appendix A: The adjoint formalism

A.1. The biorthogonality relation

We consider a continuous linear operator H with eigenvalues λ_i and eigenvectors Ψ_i linked by

$$H\Psi_i = \lambda_i\Psi_i. \quad (\text{A.1})$$

The operator H^\dagger is its adjoint with eigenvalues μ_i and eigenvectors Φ_i as

$$H^\dagger\Phi_i = \mu_i\Phi_i. \quad (\text{A.2})$$

Using the selected inner product (8), we have

$$\langle \Psi_j, H^\dagger\Phi_i \rangle = \mu_i\langle \Psi_j, \Phi_i \rangle, \quad (\text{A.3})$$

that implies

$$\langle H\Psi_j, \Phi_i \rangle = \mu_i\langle \Psi_j, \Phi_i \rangle, \quad (\text{A.4})$$

by using the adjoint definition (9). We thus obtain

$$(\lambda_j^* - \mu_i)\langle \Psi_j, \Phi_i \rangle = 0 \quad \text{hence} \quad \langle \Psi_j, \Phi_i \rangle = \delta_{ij}. \quad (\text{A.5})$$

This property is the *biorthogonality* satisfied by both the regular and adjoint eigenfunctions (e.g. Löwdin 1983).

A.2. The derivation of the adjoint matrix A^\dagger

The relation (9) that links an operator with its adjoint takes the following form in our problem

$$\int_0^1 (T'_2 \ u_2 \ R_2)^* A \begin{pmatrix} T'_1 \\ u_1 \\ R_1 \end{pmatrix} dz = \int_0^1 (T'_1 \ u_1 \ R_1) A^\dagger \begin{pmatrix} T'_2 \\ u_2 \\ R_2 \end{pmatrix} dz, \quad (\text{A.6})$$

where $(T'_2 \ u_2 \ R_2)^T$ is an adjoint eigenvector and $(T'_1 \ u_1 \ R_1)^T$ is a regular one. To determine the adjoint operator A^\dagger , we calculate each element successively from the regular matrix in Eq. (7). We provide below an example of such a calculation for the first column of the adjoint matrix given in Eq. (16).

• Calculation of A_{11}^\dagger

A_{11}^\dagger comes from the following inner-product

$$I = \langle T'_2, A_{11}T'_1 \rangle = \int_0^1 T_2'^* \frac{\gamma}{\rho_0} [K_0 D^2 + 2DK_0 D + D^2 K_0] T_1' dz. \quad (\text{A.7})$$

This integral is split in 3 parts as

$$I = \gamma \left[\underbrace{\int_0^1 \frac{T_2'^* K_0}{\rho_0} \frac{dT_1'}{dz^2} dz}_{(1)} + 2 \underbrace{\int_0^1 \frac{T_2'^*}{\rho_0} \frac{dK_0}{dz} \frac{dT_1'}{dz} dz}_{(2)} + \underbrace{\int_0^1 \frac{T_2'^*}{\rho_0} \frac{d^2 K_0}{dz^2} T_1' dz}_{(a)} \right]. \quad (\text{A.8})$$

(1) and (2) are integrated by parts, leading to

$$(1) = \left[\frac{T_2'^* K_0}{\rho_0} \frac{dT_1'}{dz} \right]_0^1 - \left[\frac{d}{dz} \left(\frac{T_2'^* K_0}{\rho_0} \right) T_1' \right]_0^1 + \underbrace{\int_0^1 \frac{d^2}{dz^2} \left(\frac{T_2'^* K_0}{\rho_0} \right) T_1' dz}_{(b)} \quad (\text{A.9})$$

$$(2) = 2 \left[\frac{T_2'^*}{\rho_0} \frac{dK_0}{dz} T_1' \right]_0^1 - 2 \underbrace{\int_0^1 \frac{d}{dz} \left(\frac{T_2'^*}{\rho_0} \frac{dK_0}{dz} \right) T_1' dz}_{(c)}.$$

While letting aside in a first step the integrated terms, the three terms (a)–(c) imply that

$$(a) + (b) + (c) = \int_0^1 T_1' \frac{\gamma K_0}{\rho_0} \{ D^2 - 2D \ln \rho_0 - D^2 \ln \rho_0 + (D \ln \rho_0)^2 \} T_2'^* dz = \langle H^\dagger T_2', T_1' \rangle. \quad (\text{A.10})$$

Applying Eq. (A.10), we finally get

$$A_{11}^\dagger = \frac{\gamma K_0}{\rho_0} \{ D^2 - 2D \ln \rho_0 D - D^2 \ln \rho_0 + (D \ln \rho_0)^2 \}. \quad (\text{A.11})$$

• Calculation of A_{21}^\dagger

A_{21}^\dagger comes from the following inner-product

$$\langle T_2', A_{12} u_1 \rangle = \int_0^1 T_2'^* \left[\frac{F_{\text{bot}}}{K_0} - (\gamma - 1) T_0 D \right] u_1 dz. \quad (\text{A.12})$$

Integrating by parts implies that

$$\langle T_2', A_{12} u_1 \rangle = \left\langle \left[(\gamma - 1) T_0 D + (2 - \gamma) \frac{F_{\text{bot}}}{K_0} \right] T_2', u_1 \right\rangle - \underbrace{(\gamma - 1) [T_2'^* T_0 u_1]_0^1}_{=0}. \quad (\text{A.13})$$

Using Eq. (5), the integrated part cancels and we obtain

$$A_{21}^\dagger = (\gamma - 1) T_0 D + (2 - \gamma) \frac{F_{\text{bot}}}{K_0}. \quad (\text{A.14})$$

• Calculation of A_{31}^\dagger

Because $A_{13} = 0$ in Eq. (7), we have

$$\langle T_2', A_{13} R_1 \rangle = 0, \quad (\text{A.15})$$

and therefore

$$A_{31}^\dagger = 0. \quad (\text{A.16})$$

A.3. The boundary conditions satisfied by A^\dagger

To determine the boundary conditions for the adjoint problem, we follow a method used in Bohlius et al. (2007). Equation (A.9) contains the boundary conditions on temperature because the definition of the adjoint operator (9) imposes that every integrated term vanishes as

$$(1) + (2) = \left[\frac{T_2'^* K_0}{\rho_0} \frac{dT_1'}{dz} \right]_0^1 + 2 \left[\frac{T_2'^*}{\rho_0} \frac{dK_0}{dz} T_1' \right]_0^1 - \left[\frac{d}{dz} \left(\frac{T_2'^* K_0}{\rho_0} \right) T_1' \right]_0^1 = 0. \quad (\text{A.17})$$

Applying Eq. (5), this equation implies the two following boundary conditions on temperature:

– At the top $z = 1$:

$$\frac{T_2'^* K_0}{\rho_0} \frac{dT_1'}{dz} = 0 \iff T_2' = 0. \quad (\text{A.18})$$

– At the bottom $z = 0$:

$$\left[2 \frac{T_2'^*}{\rho_0} \frac{dK_0}{dz} - \frac{d}{dz} \left(\frac{T_2'^* K_0}{\rho_0} \right) \right] T_1' = 0, \quad (\text{A.19})$$

which simplifies to

$$K_0 \frac{dT_2'}{dz} - \left(\frac{dK_0}{dz} + K_0 \frac{d \ln \rho_0}{dz} \right) T_2' = 0. \quad (\text{A.20})$$

References

- Aikawa, T., & Whitney, C. A. 1984, ApJ, 282, 527
Aikawa, T., & Whitney, C. A. 1985, ApJ, 296, 165
Bogdan, T. J., Cattaneo, F., & Malagoli, A. 1993, ApJ, 407, 316 (BCM93)
Bohlius, S., Pleiner, H., & Brand, H. R. 2007, Phys. Fluids, 19, 094103
Bono, G., Castellani, V., & Marconi, M. 2002, ApJ, 565, L83
Bono, G., Marconi, M., & Stellingwerf, R. F. 2000, A&A, 360, 245
Brandenburg, A., & Dobler, W. 2002, CoPhC, 147, 471
Buchler, J. R., & Goupil, M.-J. 1984, ApJ, 279, 394
Buchler, J. R., Moskalik, P., & Kovacs, G. 1990, ApJ, 351, 617
Christy, R. F. 1968, QJRAS, 9, 13
Dintrans, B., & Brandenburg, A. 2004, A&A, 421, 775
Dintrans, B., Brandenburg, A., Nordlund, Å., & Stein, R. F. 2005, A&A, 438, 365
Fadeyev, Y. A., & Muthsam, H. 1992, A&A, 260, 195
Gastine, T., & Dintrans, B. 2008, A&A, 484, 29 (Paper I)
Hertzsprung, E. 1926, Bull. Astron. Inst. Netherlands, 3, 115
Jones, E., Oliphant, T., Peterson, P., et al. 2001–2008, SciPy: open source scientific tools for Python, <http://www.scipy.org/>
Klapp, J., Goupil, M. J., & Buchler, J. R. 1985, ApJ, 296, 514
Kovacs, G., & Buchler, J. R. 1989, ApJ, 346, 898
Löwdin, P.-O. 1983, J. Math. Phys., 24, 70
Payne-Gaposchkin, C. 1954, Annals of Harvard College Observatory, 113, 151
Press, W. H., Teukolsky, S. A., Vetterling, W. T., & Flannery, B. P. 1992, Numerical recipes in FORTRAN, The art of scientific computing (Cambridge: University Press), 2nd edn.
Salwen, H., & Grosch, H. E. 1981, J. Fluid Mech., 104, 445
Simon, N. R., & Lee, A. S. 1981, ApJ, 248, 291
Simon, N. R., & Schmidt, E. G. 1976, ApJ, 205, 162, SS76
Tsvetkov, T. G. 1990, Ap&SS, 173, 31
Valdettaro, L., Rieutord, M., Braconnier, T., & Fraysse, V. 2007, JCoAM, 205, 382
Wang, M., Freund, J. B., & Lele, S. K. 2006, Ann. Rev. Fluid Mech., 38, 483
Whitney, C. A. 1956, AJ, 61, 192
Whitney, C. A. 1983, ApJ, 274, 830
Wuchterl, G., & Feuchtinger, M. U. 1998, A&A, 340, 419
Yecko, P. A., Kolláth, Z., & Buchler, J. R. 1998, A&A, 336, 553